

Mixed formulations for stress-assisted diffusion problems in cardiac biomechanics

Alessio Gizzi

Assistant Professor
Department of Engineering
University Campus Bio-Medico
Rome, Italy
A.Gizzi@unicampus.it

Adrienne Propp

DPhil Student
Mathematical Institute
University of Oxford
Oxford, United Kingdom
Propp@maths.ox.ac.uk

Ricardo Ruiz-Baier

Assistant Professor
Mathematical Institute
University of Oxford
Oxford, United Kingdom
RuizBaier@maths.ox.ac.uk

Key words : Mixed-primal formulations; stress-assisted diffusion equations; cardiac electromechanics; finite element schemes.

AMS Mathematics Subject Classification : 65M60; 92C10; 74S05; 74F99; 74D10.

Abstract : We propose and analyse the properties of a new class of models for the electromechanics of the cardiac tissue. The set of governing equations consists of nonlinear elasticity using an orthotropic exponential constitutive law coupled with a four-variable phenomenological model for human action potential. The conductivities in the model of electric propagation are modified according to stress, inducing an additional degree of nonlinearity and anisotropy in the coupling mechanisms; and the activation model assumes a simplified stretch-calcium interaction generating active tension. The influence of the new terms in the electromechanical model is evaluated through a sensitivity analysis, and we provide numerical validation through a set of computational tests using a novel mixed-primal finite element scheme.

1 Introduction

The development of complex multi-scale and multi-physics models, accompanied by advances in simulation and imaging techniques, has enabled researchers to investigate the many different aspects of cardiac function and disease. The hope is that the knowledge gained from these models can contribute to new and improved treatment methods. Even though the problem of cardiac electromechanics has been the focus of a large number of modelling and computational studies, there still remain many challenges in the development of more accurate and detailed models and the accompanying methods.

In such a context the large majority of the proposed approaches rely on continuum formulations of the complex microstructural interactions occurring among the heart tissue components, e.g. cardiomyocytes, involving different scales [32]. The study of single cell and cell-cell [27] chemomechanical and electromechanical interactions has attempted to unveil some of the underlying complex features of the cardiac function, and different multi-field nonlinear models have been gradually generalising classical approaches as the monodomain equations and Fick's diffusion. In particular, fractional diffusion [11], nonlinear and stress-assisted diffusion formulations [6] were recently proposed to reproduce porous multiscale excitation phenomena within the framework of homogenised models for cardiac tissue. These studies, in fact, paved the root towards new challenging theoretical and computational problems aiming at a reliable in silico prediction of heart rate variability, cardiac repolarisation and inducibility of life-threatening arrhythmias.

A distinguishing feature of our approach is the introduction of the mechano-electrical feedback (MEF) in the electric conductivities, through a direct dependence on the Kirchhoff stress. This framework, known as stress-assisted diffusion (SAD), is widely employed in the modelling of gels and polymers [23], but has only recently been adapted for active biological media undergoing reaction-diffusion excitation [6],

and more tailored for cardiac models in [28]. While these contributions consider hyperelastic formulations coupled with multiphysics active dynamics, and using realistic ventricular geometries. Furthermore, our model incorporates a three-field elasticity formulation that states the governing equations in terms of stress-displacement-pressure, and that is motivated by the desire to avert volumetric locking and to solve directly for additional variables of interest. In particular, we solve for the Kirchhoff stress, which we use explicitly in our incorporation of SAD. This formulation includes a pressure-stabilisation term needed in the lowest-order case $l = 0$ for triangular or for tetrahedral meshes. It constitutes a generalisation of the three-field formulation for nearly incompressible hyperelasticity, designed in [5] using quadrilateral meshes. Another difference in the present contribution is that we employ a more accurate cellular model, tailored for recovering human action potential dynamics, restitution features under constant pacing as well as sustained fibrillation behaviours and spiral waves breakup [3]. Related, numerically-oriented, studies for cardiac electromechanics include e.g. [9, 10, 14, 29, 37].

The contents of the paper have been structured in the following manner. Section 2 lays out the elements of the mathematical model that describes the electro-elastic function of the heart, including the active contraction of the cardiac muscle and the representation of the mechano-electrical feedback using stress-assisted conductivity, as well as a contribution from geometric nonlinearities. The specific structure of the governing equations suggests to cast the problem in mixed-primal form, and to use a mixed-primal finite element method for its numerical approximation. This is precisely the method that we outline in Section 3, which also includes a description of the consistent linearisation and implementation details. Our computational results in 2D and 3D, along with numerical validation and pertinent discussions on the modelling considerations are then presented in Section 4.

2 Mathematical model

2.1 Finite-strain cardiac mechanics

Let $\Omega \subset \mathbb{R}^d$, $d \in \{2, 3\}$ denote a deformable body with piecewise smooth boundary $\partial\Omega$, regarded in its reference configuration, and let n denote the outward unit normal vector on $\partial\Omega$. The kinematical description of finite deformations regarded on a time interval $t \in (0, t_{\text{final}}]$ is made precise as follows. A material point in Ω is denoted by x , whereas $u(t) : \Omega \rightarrow \mathbb{R}^d$ will denote the displacement field defining its new position in the deformed configuration. The tensor $\mathbf{F} := \mathbf{I} + \nabla u$ is the gradient (applied with respect to the fixed material coordinates) of the deformation map; its Jacobian determinant, denoted by $J = \det \mathbf{F}$, measures the solid volume change during the deformation; and $\mathbf{C} = \mathbf{F}^\top \mathbf{F}$ and $\mathbf{B} = \mathbf{F} \mathbf{F}^\top$ are respectively the right and left Cauchy-Green deformation tensors on which all strain measures will be based (here the superscript $(\cdot)^\top$ denotes the transpose operator). The first isotropic invariant ruling deviatoric effects is the scalar $I_1(\mathbf{C}) = \text{tr} \mathbf{C}$, and for generic unitary vectors f_0, s_0 , the scalars $I_{4,f}(\mathbf{C}) = f_0 \cdot (\mathbf{C} f_0)$, $I_{4,s}(\mathbf{C}) = s_0 \cdot (\mathbf{C} s_0)$, $I_{8,fs}(\mathbf{C}) = f_0 \cdot (\mathbf{C} s_0)$ are pseudo-invariants of \mathbf{C} measuring direction-specific stretch [7].

The triplet $(f_0(x), s_0(x), n_0(x))$ represents a coordinate system pointing in the local direction of the muscular cardiac fibres, transversal sheetlet compound, and normal cross-fibre direction $n_0(x) = f_0(x) \times s_0(x)$. Note that the system is restricted to $(f_0(x), s_0(x))$ in the two-dimensional case, and that these directions are defined in the reference configuration. Constitutive relations characterising the material properties and underlying microstructure of the myocardial tissue will follow the orthotropic model proposed in [19], whose strain energy function and the first Piola-Kirchhoff stress tensor (associated with a passive, elastic deformation and having units [Pa]) read, respectively

$$\begin{aligned} \Psi_{\text{pas}}(\mathbf{F}) &= \frac{a}{2b} e^{b(I_1-d)} + \sum_{i \in \{f,s\}} \frac{a_i}{2b_i} [e^{b_i(I_{4,i}-1)_+^2} - 1] + \frac{a_{fs}}{2b_{fs}} [e^{b_{fs}(I_{8,fs})^2} - 1], \\ \mathbf{P}_{\text{pas}} &= \frac{\partial \Psi_{\text{pas}}}{\partial \mathbf{F}} - p \mathbf{J} \mathbf{F}^{-\top}, \end{aligned} \tag{2.1}$$

where a, b are material constants associated with the isotropic matrix response, a_f, b_f rule the directional behaviour of the material along myocardial fibres, a_s, b_s account for the cross-contribution of the fibre sheet

directions, and a_{fs}, b_{fs} encapsulate the shear effects in the sheet plane. Moreover, the field p denotes the solid hydrostatic pressure, and we have used the notation $(u)_+ := u$ if $u > 0$ or zero otherwise, for a generic real-valued function u .

2.2 Active stress

We assume that the first Piola-Kirchhoff stress tensor decomposes as

$$\mathbf{P} = \mathbf{P}_{\text{pas}} + \mathbf{P}_{\text{act}}, \quad (2.2)$$

where the active stress component acts differently on each local direction with an intensity depending on the scalar field of active tension T_a , that synthesises the biochemical state of myocytes (and whose dynamic behaviour will be specified later on), so that

$$\mathbf{P}_{\text{act}} = J\sigma_{\text{act}}\mathbf{F}^{-\text{t}}, \quad \text{with} \quad \sigma_{\text{act}} = \frac{T_a}{J\lambda_f}\mathbf{F}f_0 \otimes \mathbf{F}f_0 + \frac{\kappa_{sn}T_a}{J\lambda_s\lambda_n}\text{sym}(\mathbf{F}s_0 \otimes \mathbf{F}n_0) + \frac{\kappa_{mn}T_a}{J\lambda_n}\mathbf{F}n_0 \otimes \mathbf{F}n_0, \quad (2.3)$$

where κ_{sn}, κ_{mn} are positive constants representing the variation of activation on each specific direction, as proposed in [12], and $\lambda_f = \sqrt{I_{4,f}}, \lambda_s = \sqrt{I_{4,s}}, \lambda_n = \sqrt{n_0 \cdot (\mathbf{C}n_0)}$ are the fibre, sheetlet, and cross-fibre stretches. Setting appropriate models for σ_{act} is not a trivial task since the active contribution to the force should account for the geometric properties of deformation, and these undergo substantial changes during contraction in the finite strain regime [31]. Details of other anisotropic activation forms can be found, for instance, in [38, Appendix B] for active stress descriptions, but they are basically responsible for additional deformation effects such as wall thickening, radial constriction and torsion, as well as longitudinal shortening. Note that the active Cauchy stress does not include a contribution on the diagonal entry associated with the local sheetlet alignment s_0 since a stress component on this direction would counteract wall thickening mechanisms [12]. Moreover, the intensity of the active tension effect on the cross-fibre direction n_0 is assumed substantially smaller than that appearing on the off-diagonal component $\text{sym}(\mathbf{F}s_0 \otimes \mathbf{F}n_0)$, see Table II. Also note that some references do not include a rescaling with local stretches in each term of σ_{act} .

2.3 Viscoelasticity and equations of motion

Extension and shear tests demonstrate the importance of incorporating viscoelastic effects in models for cardiac passive mechanics [16]. In the heart, the extracellular fluid filtrating through the elastic solid is one of the main generators of the viscoelastic effects of the tissue [39]. These effects could also be tied to the molecule titin in the tissue, and have a well-established literature as well as a consistent methodology (the stress update algorithm that uses a convolution integral representation) developed for general soft tissues [18]. From the viewpoint of kinematics, it suffices to relate stress to strain rates. Decomposition of the spatial velocity gradient $w = \dot{u}$ into the rate of deformation and spin tensors yields the relation

$$\dot{\mathbf{B}} = \nabla_w \mathbf{B} + \mathbf{B}(\nabla w)^{\text{t}},$$

and a simplified rheological Kelvin-Voigt model for the viscous component of the Cauchy stress can be defined as follows (see e.g. [21])

$$\sigma_{\text{visc}} = \delta e^{\beta I_1} \dot{\mathbf{B}}, \quad (2.4)$$

which depends on the history of the isotropic contribution to the Cauchy stress, and can be associated with e.g. the structure of the extracellular matrix. Here $\delta, \beta > 0$ are model parameters. In this way, after a pull-back operation we see that

$$\mathbf{P}_{\text{tot}} = \mathbf{P} + J\sigma_{\text{visc}}\mathbf{F}^{-\text{t}}, \quad (2.5)$$

is the total first Piola-Kirchhoff stress tensor that includes \mathbf{P} defined from (2.1)-(2.2), and the viscoelastic contributions.

More advanced rheologies can be easily incorporated in the context of active stress formulations as done in e.g. [22], as the generalised Hill-Maxwell model recently proposed in [4]. We will, however, confine the presentation to (2.5) without introducing stochasticity of the anisotropic components.

The balance of linear momentum and the incompressibility constraint (allowing only isochoric motions) are written together in the following way, when posed in the inertial reference frame and under transient mechanical equilibrium,

$$\rho \partial_t u - \nabla \cdot \mathbf{P}_{\text{tot}} = \rho_0 b \quad \text{in } \Omega \times (0, t_{\text{final}}], \quad (2.6a)$$

$$\rho J - \rho_0 = 0 \quad \text{in } \Omega \times (0, t_{\text{final}}], \quad (2.6b)$$

where ρ_0, ρ are the reference and current medium density, b is a smooth vector field of imposed body loads, and the divergence operator in (2.6a) applies on the tensor fields row-by-row. The balance of angular momentum translates into the condition that the Kirchhoff stress tensor $\Pi = \mathbf{P}_{\text{tot}} \mathbf{F}^t$ must be symmetric, which is in turn encapsulated into the momentum and constitutive relations (2.6a), (2.1), (2.3).

Defining

$$\mathcal{G} = \mathcal{G}(u, T_a) := \frac{\partial \Psi}{\partial \mathbf{F}} \mathbf{F}^t + J \sigma_{\text{visc}} + \mathbf{P}_{\text{act}} \mathbf{F}^t,$$

as the contribution to the Kirchhoff stress that does not involve pressure, we then have

$$\Pi = \mathcal{G} - p \mathbf{I}. \quad (2.7)$$

Stating the balance equations in terms of Kirchhoff stress, displacements, and pressure suggests that, at the level of writing finite element schemes, we will use mixed methods respecting the same structure. Setting boundary conditions for the motion of the left ventricle is not trivial, as the organ is known to slightly move and twist during the heartbeat. In our case, equations (2.6a)-(2.6b)-(2.7) will be supplemented with mixed normal displacement and traction boundary conditions

$$u \cdot n = 0 \quad \text{on } \partial \Omega_D \times (0, t_{\text{final}}], \quad (2.8a)$$

$$\Pi \mathbf{F}^{-t} n = p_N J \mathbf{F}^{-t} n \quad \text{on } \partial \Omega_N \times (0, t_{\text{final}}], \quad (2.8b)$$

$$\Pi \mathbf{F}^{-t} n + \eta J \mathbf{F}^{-t} u = 0 \quad \text{on } \partial \Omega_R \times (0, t_{\text{final}}], \quad (2.8c)$$

where $\partial \Omega_D, \partial \Omega_N, \partial \Omega_R$ conform a disjoint partition of the boundary. The term p_N denotes a boundary pressure associated with endocardial blood pressure, which is uniform over the deformed counterpart of $\partial \Omega_N$ and it is applied in the current normal direction, and this contribution regarded on the reference configuration depends on the cofactor of the deformation gradient. A sketch of a mono-ventricular domain with specification of boundary surfaces and fibre directions is depicted in Figure 1.

2.4 Monodomain equations

The propagation of electric potential v , in the reference configuration, is governed by the following reaction-diffusion system, known as the monodomain equations (see e.g. [8]). Current conservation is written only in terms of the transmembrane potential and a coupling with additional ionic quantities encoded in \vec{r}

$$\chi \frac{\partial v}{\partial t} - \nabla \cdot \{ \mathbf{D}(v, \mathbf{F}, \Pi) \nabla v \} = g(v, \vec{r}) + I_{\text{ext}} \quad \text{in } \Omega \times (0, t_{\text{final}}], \quad (2.9a)$$

$$\frac{d\vec{r}}{dt} = \vec{m}(v, \vec{r}) \quad \text{in } \Omega \times (0, t_{\text{final}}]. \quad (2.9b)$$

Here χ is the ratio of membrane area per tissue volume, and I_{ext} is a spatio-temporal external stimulus applied to the medium. We will adopt the minimal model for human ventricular action potential, proposed in [3] and fitted to capture restitution curves, conduction velocity, spiral/arrhythmic dynamics, and complex behaviour typical to nonlinear dynamical systems. The ionic currents consist of three general terms, phenomenologically constructed (without particularisation to the ionic species that carry them)

$$g(v, \vec{r}) = g^{\text{fi}}(v, \vec{r}) + g^{\text{si}}(v, \vec{r}) + g^{\text{so}}(v, \vec{r}),$$

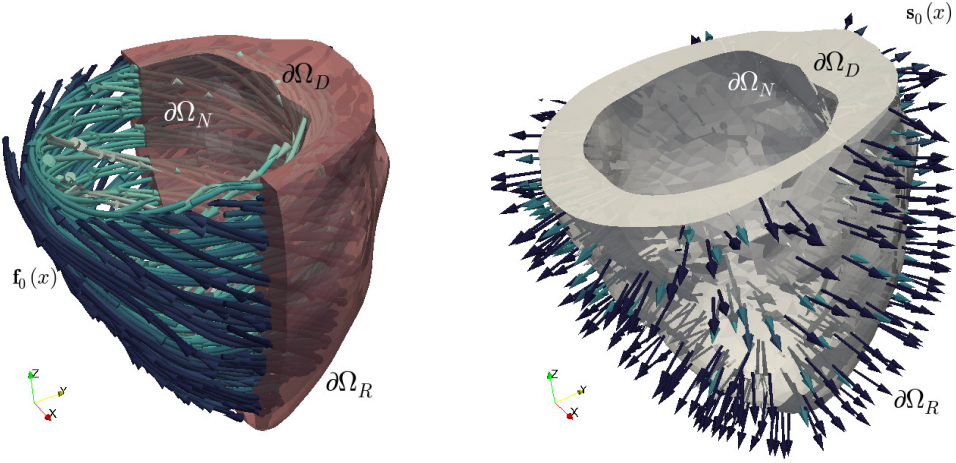


Fig. 1: Schematic representation of a mono-ventricular domain where (2.8a) is imposed on the basal cut, (2.8b) on the endocardial surface, and (2.8c) on the epicardium. The left panel depicts the fibre field and the right panel the sheetlets.

where the adimensional *fast inward*, *slow inward* and *slow outward* currents are respectively given by

$$\begin{aligned}\chi g^{\text{fi}}(v, \vec{r}) &= -r_1 \mathcal{H}(v - \theta_1)(v - \theta_1)(v_v - v) / \tau_{fi}, \\ \chi g^{\text{si}}(v, \vec{r}) &= -\mathcal{H}(v - \theta_2)r_2 r_3 / \tau_{si}, \\ \chi g^{\text{so}}(v, \vec{r}) &= (v - v_0)(1 - \mathcal{H}(v - \theta_2)) / \tau_o + \mathcal{H}(v - \theta_2) / \tau_{so},\end{aligned}$$

and the kinetics of the gating variables \vec{r} are given by

$$\vec{m}(v, \vec{r}) = \begin{pmatrix} (1 - \mathcal{H}(v - \theta_1))(r_{1,\text{inf}} - r_1) / \tau_1^- - \mathcal{H}(v - \theta_1)r_1 / \tau_1^+ \\ (1 - \mathcal{H}(v - \theta_2))(r_{2,\text{inf}} - r_2) / \tau_2^- - \mathcal{H}(v - \theta_2)r_2 / \tau_2^+ \\ ((1 + \tanh(k_3(v - v_3))) / 2 - r_3) / \tau_3 \end{pmatrix}.$$

Here \mathcal{H} is the Heaviside step function, and the time constants and steady-state values are defined as:

$$\begin{aligned}\tau_1^- &= (1 - \mathcal{H}(v - \theta_1^-))\tau_{1,1}^- + \mathcal{H}(v - \theta_1^-)\tau_{1,2}^-, & \tau_2^- &= \tau_{2,1}^- + (\tau_{2,2}^- - \tau_{2,1}^-)(1 + \tanh(k_2^-(v - v_2^-))) / 2 \\ \tau_{so} &= \tau_{so,1} + (\tau_{so,2} - \tau_{so,1})(1 + \tanh(k_{so}(v - v_{so}))) / 2 \\ \tau_3 &= ((1 - \mathcal{H}(v - \theta_2))\tau_{3,1} + \mathcal{H}(v - \theta_2)\tau_{3,2}), & \tau_o &= ((1 - \mathcal{H}(v - \theta_0))\tau_{o,1} + \mathcal{H}(v - \theta_0)\tau_{o,2}) \\ r_{1,\text{inf}} &= \begin{cases} 1, & v < \theta_1^- \\ 0, & v \geq \theta_1^- \end{cases}, & r_{2,\text{inf}} &= ((1 - \mathcal{H}(v - \theta_0))(1 - v / \tau_{2,\infty}) + \mathcal{H}(v - \theta_0)r_{2,\infty}^*.\end{aligned}$$

Boundary and initial conditions for (2.9) correspond to

$$\mathbf{D}(v, \mathbf{F}, \Pi) \nabla v \cdot \mathbf{n} = 0 \quad \text{on } \partial\Omega \times (0, t_{\text{final}}], \quad (2.10a)$$

$$v(0) = 0, \quad \vec{r} = [1, 1, 0] \quad \text{in } \Omega \times \{0\}. \quad (2.10b)$$

2.5 Stress-assisted conduction

The mechano-electrical feedback (the process where the current mechanical state of the deforming solid modifies both the excitability and electrical conduction of the tissue) is here introduced in the conductivity tensor, through a direct dependence on the Kirchhoff stress (which constitutes one of the main novelties in our approach, stemming as a generalisation of the anisotropy induced by stress proposed in [6] and later exploited for simplified 2D cardiac electromechanics in [28]). In addition, due to the Piola transformation

(forcing a compliance of the diffusion tensor using the deformation gradients), the conductivity tensor also depends nonlinearly on the deformation gradient (actually, the term $J\mathbf{C}^{-1}$ constitutes a strain-enhanced tissue conductivity, also referred to as geometric feedback in [9])

$$\mathbf{D}(v, \mathbf{F}, \Pi) = [D_0 + D_1 v] J \mathbf{C}^{-1} + D_0 / 2 J f_0 \otimes f_0 + D_2 J \mathbf{F}^{-1} \Pi \mathbf{F}^{-t}, \quad (2.11)$$

where the nonlinear conductivity (self diffusion depending on v) accounts for porous media electrophysiology following the development in [20], but appropriately modified to incorporate information about preferred directions of diffusivity according to the microstructure of the tissue (encoded in the second term defining \mathbf{D}). The parameter D_0 carries the usual diffusion for isotropic materials, whereas D_1 and D_2 represent the intensity of the porous media electrophysiology and of the stress-assisted diffusion, respectively. An additional term in the nonlinear self-diffusion (e.g. $D_3 v^2$, as in [35]) eventually leads to very slight modifications in conduction patterns and we have therefore decided not to include it. Tuning D_1 is sufficient to, if needed, calibrate the speed and action potential duration at the depolarisation plateau phase.

2.6 Activation mechanisms and excitation-contraction coupling

When using the active stress approach, we will adopt a simple description where the active tension is generated by ionic quantities (calcium) as well as by local fibre stretch. That is, we propose a regularised active tension model of the form

$$\partial_t T_a = \hat{\alpha} \Delta T_a + \ell(T_a, \vec{r}, I_{4,f}) \quad \text{in } \Omega \times (0, t_{\text{final}}], \quad (2.12)$$

with $\hat{\alpha} = \alpha_1 D_0$ and $\alpha_1 > 0$ a model constant. As calcium concentration is not readily available in the phenomenological cellular model we are employing, we use r_3 as a proxy for intracellular calcium [3].

3 Numerical approximation and implementation

The spatial discretisation will follow a mixed-primal Galerkin approach, restricting the presentation to the active stress formulation using a smoothed model for active tension. Let us denote by \mathcal{T}_h a regular partition of Ω into simplicial elements K (pair-wise disjoint triangles in 2D or tetrahedra in 3D) of maximum diameter h_K , and define the meshsize as $h := \max\{h_K : K \in \mathcal{T}_h\}$. Let us also denote by \mathcal{E}_h the set of interior facets of the mesh, and by $[[\cdot]]_e$ the jump of a quantity across a given facet $e \in \mathcal{E}_h$. The specific finite element method we use here is based on solving the discrete weak form of the hyperelasticity equations using piecewise constant approximations of the symmetric Kirchhoff stress tensor, piecewise linear approximation of displacements, and piecewise constant approximation of solid pressure. The transmembrane potential in the electrophysiology equations is discretised with Lagrange finite elements (piecewise linear and continuous functions), and the remaining ionic quantities are approximated by piecewise constant functions. More precisely, we use the finite dimensional spaces $\mathbb{H}_h \subset \mathbb{L}_{\text{sym}}^2(\Omega)$, $\mathbf{V}_h \subset \mathbf{H}^1(\Omega)$, $W_h \subset H^1(\Omega)$, $Q_h \subset L^2(\Omega)$, $Z_h \subset L^2(\Omega)^3$ defined (for the case of a generic-order approximation $l \geq 0$) as follows:

$$\begin{aligned} \mathbb{H}_h &:= \{\boldsymbol{\tau}_h \in \mathbb{L}_{\text{sym}}^2(\Omega) : \boldsymbol{\tau}_h|_K \in \mathbb{P}_l(K)^{d \times d}, \forall K \in \mathcal{T}_h\}, \\ \mathbf{V}_h &:= \{v_h \in \mathbf{H}^1(\Omega) : v_h|_K \in \mathbb{P}_{l+1}(K)^d, \forall K \in \mathcal{T}_h, \quad v_h \cdot n = 0 \text{ on } \partial\Omega_D\}, \\ Q_h &:= \{q_h \in L^2(\Omega) : q_h|_K \in \mathbb{P}_l(K), \forall K \in \mathcal{T}_h\}, \\ W_h &:= \{w_h \in H^1(\Omega) : w_h|_K \in \mathbb{P}_{l+1}(K), \forall K \in \mathcal{T}_h\}, \\ Z_h &:= \{\boldsymbol{\varphi}_h \in L^2(\Omega) : \boldsymbol{\varphi}_h|_K \in \mathbb{P}_l(K), \forall K \in \mathcal{T}_h\}, \end{aligned}$$

where $\mathbb{P}_r(l)$ denotes the space of polynomial functions of degree $s \leq l$ defined locally on the element K . Assuming zero body loads, and applying a backward differentiation formula (BDF) for the time integration we end up with the following fully-discrete nonlinear electromechanical problem, starting from the discrete

initial data $v_h^0, n_h^0, T_{a,h}^0$. For each $n = 0, 1, \dots$: find $(\Pi_h^{n+1}, u_h^{n+1}, p_h^{n+1})$ and $(v_h^{n+1}, \bar{r}_h^{n+1}, T_{a,h}^{n+1})$ such that

$$\begin{aligned}
& \int_{\Omega} [\Pi_h^{n+1} - \mathcal{G}(u_h^{n+1}) + p_h^{n+1} J(u_h^{n+1}) \mathbf{I}] : \boldsymbol{\tau}_h = 0 \quad \forall \boldsymbol{\tau}_h \in \mathbb{H}_h, \\
& \int_{\Omega} \frac{u_h^{n+1} - 2u_h^n + u_h^{n-1}}{\Delta t^2} \cdot v_h + \int_{\Omega} \Pi_h^{n+1} : \nabla v_h \mathbf{F}^{-\tau}(u_h^{n+1}) - \int_{\partial\Omega_N} p_N \mathbf{F}^{-\tau}(u_h^{n+1}) u_h^{n+1} \cdot v_h = 0 \quad \forall v_h \in \mathbf{V}_h, \\
& \int_{\Omega} [J(u_h^{n+1}) - 1] q_h + \sum_{e \in \mathcal{E}_h} \int_e \frac{\zeta_{\text{stab}}}{h_e} [[p_h^{n+1}]]_e [[q_h]]_e = 0 \quad \forall q_h \in \mathcal{Q}_h, \quad (3.1) \\
& \int_{\Omega} \frac{v_h^{n+1} - v_h^n}{\Delta t} w_h + \int_{\Omega} \mathbf{D}(v_h^{n+1}, \Pi_h^{n+1}) \nabla v_h^{n+1} \cdot \nabla w_h - \int_{\Omega} \left[g(v_h^n, \bar{r}_h^n) + I_{\text{ext}} \right] w_h = 0 \quad \forall w_h \in W_h, \\
& \int_{\Omega} \frac{\bar{r}_h^{n+1} - \bar{r}_h^n}{\Delta t} \cdot \bar{s}_h - \int_{\Omega} \bar{m}(v_h^n, \bar{r}_h^n) \cdot \bar{s}_h = 0 \quad \forall \bar{s}_h \in Z_h^3, \\
& \int_{\Omega} \frac{T_{a,h}^{n+1} - T_{a,h}^n}{\Delta t} \varphi_h + \alpha_1 D_0 \int_{\Omega} \nabla T_{a,h}^{n+1} \cdot \nabla \varphi_h - \int_{\Omega} \ell(T_{a,h}^{n+1}, \bar{r}_h^n) \varphi_h = 0 \quad \forall \varphi_h \in W_h,
\end{aligned}$$

where ζ_{stab} is a positive pressure stabilisation parameter required in this tetrahedral counterpart of the finite element method for quadrilateral meshes studied in [5] and recently exploited in the context of cardiac electromechanics in [35]. Notice that the boundary condition (2.8a) is incorporated as an essential condition on the displacement space, whereas the traction boundary condition (2.8b) on the remaining of the boundary $\partial\Omega_N$ appears naturally as the last term in the second equation of (3.1).

The motivation for using three-field elasticity formulations is the need to produce conservative solutions with balanced convergence orders for all variables. In addition, these methods are robust in the incompressible regime; they are not subject to volumetric locking [25]; and most importantly, they provide direct approximation of variables of interest, nonetheless at a higher computational cost. Another advantage of using the Kirchhoff stress is that this tensor is symmetric, and, for simpler material laws, is a polynomial function of the displacements (whereas first and second Piola-Kirchhoff stresses are rational functions of displacement) [5]. Alternative remedies for overcoming locking include non-conforming methods (as discussed for the case of cardiac biomechanics in [2]), high order elements and stabilised mixed formulations [36], or Lagrange multiplier-based methods [17]. In our case, solving in terms of stresses proves particularly useful, as this variable participates actively in the electromechanical coupling through the stress-assisted diffusion. Moreover, for the lowest-order method characterised by $l = 0$, the matrix system associated with (3.1) has fewer unknowns than the discretisation that uses piecewise quadratic and continuous displacement approximations and piecewise linear and discontinuous pressure approximations (and which is a popular locking-free scheme for hyperelasticity in the displacement-pressure formulation, exploited for stress-assisted diffusion problems in the recent work [28]). The importance of casting the equations of motion in terms of the coupling variables has been already emphasized in [34] in the context of cardiac electromechanics, where it is shown that the computation of output indicators of interest (such as conduction velocities) may suffer from a loss of accuracy up to 23% if one simply postprocesses stress or strain from discrete displacements as approximations in the geometric feedback.

According to the fixed-point separation between electrophysiology and viscoelastic solvers, the nonlinear mechanics will be solved using the embedded Newton-Raphson method stated above, and an operator splitting algorithm will separate an implicit diffusion solution (where another Newton iteration handles the nonlinear self-diffusion) from an explicit reaction step for the kinetic equations, turning the overall solver into a semi-implicit method. Such a strategy is feasible since the Jacobians associated with the reaction and excitation-contraction models do not possess highly varying eigenvalues. Updating and storing of the internal variables ξ and \bar{r} will be done locally at the quadrature points. We specify that the linear system occurring in the Newton iteration will be solved by the Krylov iterative method GMRES preconditioned with an incomplete LU(0) factorisation (except for the linear systems in the convergence tests in Section 4.1, which will be solved with the direct method SuperLU), and the iterates are terminated once a tolerance of 10^{-6} (imposed on the ℓ^∞ -norm of the non-preconditioned residual) has been achieved. The mass matrices associated with the discretisation of the monodomain equations are assembled in a lumped manner, which

(a) Hyperelasticity variables

DoF	h	$\ \Pi - \Pi_h\ _{0,\Omega}$	rate	$\ u - u_h\ _{1,\Omega}$	rate	$\ p - p_h\ _{0,\Omega}$	rate
77	0.7071	43.252	–	0.0576	–	30.161	–
253	0.3536	27.137	0.6725	0.0342	0.6345	19.030	0.6647
917	0.1768	12.535	1.1140	0.0216	0.7615	9.2110	1.0471
3493	0.0884	6.2636	1.0012	0.0118	0.8751	4.8012	0.9401
13637	0.0442	1.9169	1.1727	0.0071	0.9516	1.9631	1.3817
53893	0.0221	0.9841	0.9907	0.0042	0.9737	0.9206	0.9858

(b) Electrophysiology variables

DoF	h	$\ v - v_h\ _{1,\Omega}$	rate	$\ r - r_h\ _{1,\Omega}$	rate	$\ T_a - T_{a,h}\ _{1,\Omega}$	rate
77	0.7071	0.1528	–	0.1926	–	0.1623	–
253	0.3536	0.0902	0.7601	0.1069	0.8499	0.0847	0.8824
917	0.1768	0.0491	0.8769	0.0573	0.8968	0.0433	0.9673
3493	0.0884	0.0282	0.8016	0.0317	0.9536	0.0218	0.9896
13637	0.0442	0.0153	0.9304	0.0172	0.9612	0.0121	0.9446
53893	0.0221	0.0084	0.9587	0.0091	0.9843	0.0067	0.9562

TABLE I: Test 1: Error history (errors on a sequence of successively refined grids and convergence rates) associated with the mixed finite element method (3.1) applied to a steady-state electromechanical coupling under active stress, for the lowest-order case $l = 0$.

reduces the amount of artificial diffusion and violation of the discrete maximum principle [32]. All routines have been implemented using the finite element library FEniCS [1].

4 Computational results

4.1 Mesh convergence

A convergence test is generated by computing errors between smooth exact solutions and approximate solutions using the first-order and the second-order methods discussed in Section 3. Let us consider the following closed-form solutions to a steady-state counterpart of the electromechanics equations, also assuming the absence of viscoelastic effects, and defined on the domain $\Omega = (0, 1)^2$ with the fibres/sheetlets defined as $f_0 = (0, 1)^t, s_0 = (-1, 0)^t$

$$u(x, y) = 0.1 \begin{pmatrix} \sin(\pi x) \cos(\pi y) \\ \cos(\pi x) \sin(\pi y) \end{pmatrix}, \quad p(x, y) = 0.1 \sin(\pi x) \sin(\pi y), \quad v(x, y) = 1 + 0.1 \cos(\pi x) \cos(\pi y),$$

$$r(x, y) = 0.1 \cos(\pi x) \sin(\pi y) \sin(\pi x), \quad T_a(x, y) = 1 + 0.1 \cos(\pi x) \sin(\pi y).$$

Then the Kirchhoff stress Π , as well as suitable forcing terms (volume load, an additional external stimulus, and the active tension source) are computed from these smooth solutions, the balance equations, relations (2.2), (2.3), (2.11), and using the following simplified constitutive equations

$$m(v, r) = v - r^2, \quad g(v, r) = (v - 1)vr, \quad \ell(T_a, r) = -T_a + r.$$

Note also that the incompressibility constraint for this test is $J = J_{ex}$, where J_{ex} is computed from the exact displacement. Here we also prescribe Dirichlet boundary conditions for displacements, transmembrane potential, and active tension (incorporated in the discrete trial spaces). Errors due to fixed-point iterations are avoided by taking a full monolithic coupling and computing solutions using Newton-Raphson iterations with an exact Jacobian. On a sequence of six uniformly refined meshes, we proceed to compute errors between the exact and approximate solutions computed with the lowest-order method $l = 0$. Kirchhoff

stress and pressure errors are measured in the L^2 -norm, whereas for the remaining variables the errors are measured in the H^1 -norm. The obtained error history is reported in Table I, where we observe an asymptotic $O(h)$ decay of the error for each field variable.

Viscoelasticity constants			
$a = 0.236$ [N/cm ²]	$a_f = 1.160$ [N/cm ²]	$a_s = 3.724$ [N/cm ²]	$a_{fs} = 4.010$ [N/cm ²]
$b = 10.81$ [-]	$b_f = 14.15$ [-]	$b_s = 5.165$ [-]	$b_{fs} = 11.60$ [-]
$p_0 = 0.1$ [N/cm ²]	$\beta = 10$ [ms]	$\delta = 22.6$ [N/cm ² ms]	$\zeta_{stab} = 0.25$ [-]
$\eta_a = 0.001$ [N/cm ²]	$\eta_b = 0.01$ [N/cm ²]	$\kappa_{sn} = 0.6$ [-]	$\kappa_{mn} = 0.03$ [-]
$\rho_0 = 0.001$ [N/cm ²]			
Electrophysiology constants			
$v_0 = 0$ [-]	$v_v = 1.55$ [-]	$v_2^- = 0.03$ [-]	$v_{so} = 0.65$ [-]
$v_3 = 0.908$ [-]	$\theta_1 = 0.3$ [-]	$\theta_1^- = 0.006$ [-]	$\theta_o = 0.006$ [-]
$\theta_2 = 0.13$ [-]	$k_2^- = 65$ [-]	$k_3 = 2.099$ [-]	$k_{so} = 2.045$ [-]
$r_{1,\infty}^* = 0.94$ [-]	$\tau_{2,\infty}^- = 0.07$ [-]	$\tau_{1,1}^- = 60$ [-]	$\tau_{1,2}^- = 1150$ [-]
$\tau_{2,1}^- = 60$ [-]	$\tau_{2,2}^- = 15$ [-]	$\tau_{so} = 0.11$ [-]	$\tau_{o1} = 30.02$ [-]
$\tau_{o2} = 0.996$ [-]	$\tau_{so,1} = 2.046$ [-]	$\tau_{so,2} = 0.65$ [-]	$\tau_{3,1} = 2.734$ [-]
$\tau_{3,2} = 16$ [-]	$\tau_{so,3} = 1.888$ [-]	$\tau_1^+ = 1.451$ [-]	$\tau_2^+ = 200$ [-]
Activation and excitation-contraction coupling constants			
$D_0 = 1.171$ [cm ² /s]	$D_1 = 0.9$ [cm ² /s]	$D_2 = 0.01$ [cm ² /s]	$K_0 = 5$ [-]
$K_1 = -0.015$ [-]	$K_2 = -0.15$ [-]	$\alpha_1 = 10$ [-]	$\alpha_2 = 0.5$ [-]

TABLE II: Model parameters for the electro-viscoelastic model (2.6), (2.9), (2.12). Values are taken from [3,6,13,33], and the transmembrane potential v is in dimensionless units.

4.2 Parameter calibration

For the following 2D simulations will consider tissue slabs of 50×50 mm². The initiation, maintenance, prevention and treatment of so-called reentrant waves is a major focus of current research due to their implication in atrial and ventricular fibrillation [8]. We are thus interested in investigating the formation of spiral reentrant waves in our model setup, following the S1-S2 stimulation protocol. In our simulations, both waves have nondimensional amplitude 3 and duration 3 ms. The S2 stimulus, occurring at $t = 330$ ms and $t = 335$ ms in 2D and 3D, respectively, is a square wave in the bottom left quadrant or octant, respectively. The formation and evolution of the spiral wave on its deforming domain can be seen in Figure 2. The spiral is initiated by the diffusion of voltage and ionic entities from the S2 stimulus into the leftmost section of the tissue, which has recovered enough excitability after S1. The wave then spreads outwards in all directions, invading the entire tissue except for the region that was just excited by the S2 wave.

Next we proceed to evaluate α_1, α_2 , the parameters governing active tension in (2.12), and η , the stiffness parameter from (2.8c). We conduct a simple sensitivity analysis by increasing or decreasing either α_1, α_2 or η by one order of magnitude, holding the others constant at their reference values ($\alpha_1 = 10$, $\alpha_2 = 0.5$, and $\eta = \eta_a = 0.001$ N/cm², as listed in Table II). This simple analysis therefore does not test for compounding or competitive effects. Parameter α_1 contributes to producing smoother active tension profiles, while α_2 controls their range. These effects are visible in Figure 3. We found that larger values of α_1 produced smoother gradients in pressure and stress, while larger values of α_2 produced higher magnitude displacement, Kirchhoff stress, and pressure, as well as some more subtle changes in ionic quantities. Parameter η determines the stiffness of the springs supporting the tissue, and decreasing η resulted an increase in the magnitude of displacement, stress, and pressure, as expected. However, these differences were minimal, even across the three orders of magnitude tested ($\eta = 1E-4$ to $\eta = 0.01$). The effects on ionic entities were even smaller, for both the hyperelastic and viscoelastic cases, and therefore plots are not shown.

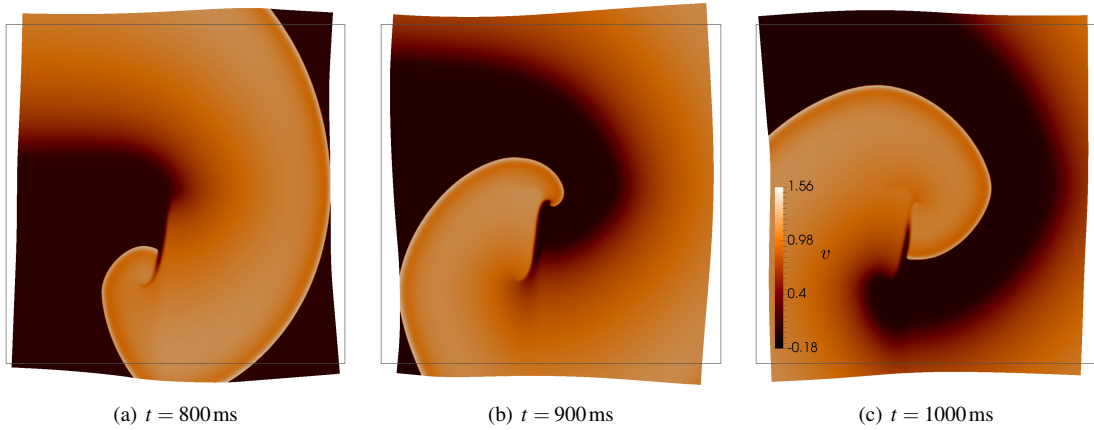


Fig. 2: Evolution of voltage after S2 stimulus, showing formation of a reentrant spiral wave on the deforming viscoelastic tissue.

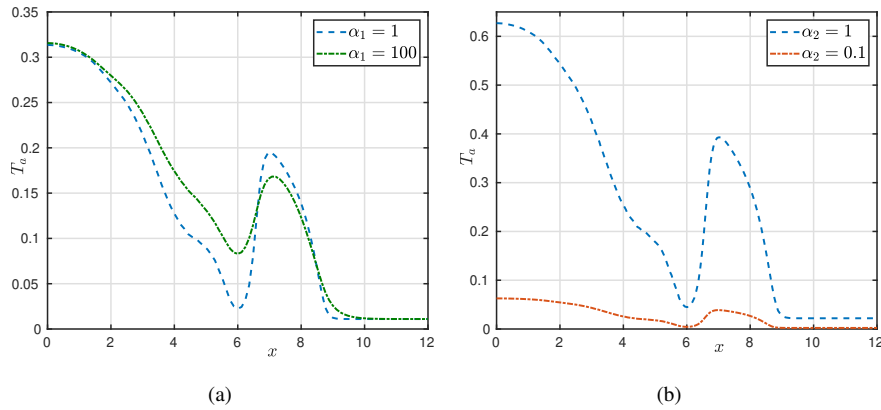


Fig. 3: Profiles of T_a taken across the tissue at $y = 6$ cm and $t = 432$ ms to evaluate the effect of parameters α_1 and α_2 .

Computational experiments reveal a window of values of D_2 for which our method converges. In the 2D hyperelastic case, we found that the upper bound for D_2 is approximately $D_2 = 2.1\text{E-}2$ cm²/s, with the linear solver failing to converge for larger values. In these simulations, the Kirchhoff stress achieved an L^2 -norm of between 0.006 and 0.6. In turn, the viscoelastic case was able to accept slightly larger values of D_2 , up to $D_2 = 2.2\text{E-}2$ cm²/s, with the L^2 -norm of stress falling between 0.001 and 0.5.

4.3 Locking-free property

We next proceed to assess the performance of the proposed mixed formulations for the mechanical problem. In this example we solve only for (2.6) without the acceleration term (otherwise present in all other simulations), using the active stress approach with a fixed value for the active tension and without the contribution from the viscous stress (2.4). We proceed to compare the deformation achieved by the mixed formulation with that of an asymptotic solution and the approximate solution generated by a more standard pressure-displacement finite element formulation. We consider different stabilisation parameter values and mesh refinements.

We consider a 3D computation suggested in [26, Test I] as a simple benchmark for passive cardiac mechanics, and so we set $T_a = 0$. The problem consists in computing the deformation of a point at the right end of a beam defined by the domain $\Omega = (0, 10) \times (0, 1) \times (0, 1)$ mm, where the fibre direction is $f_0 = (1, 0, 0)^t$. Instead of (2.1), the material is characterised by the transversally isotropic strain en-

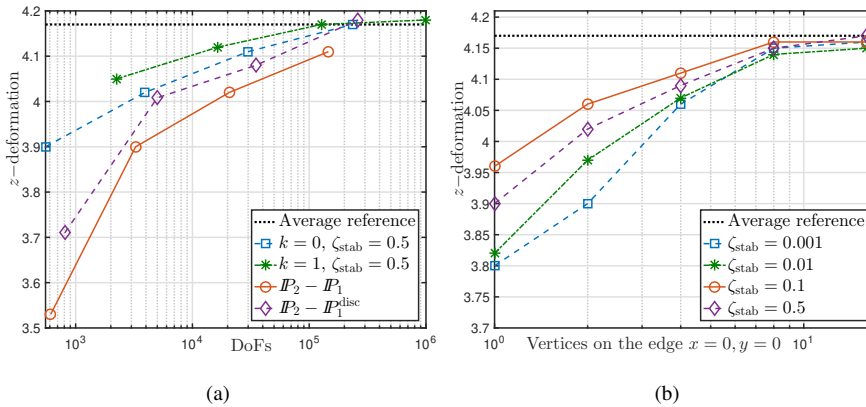


Fig. 4: Convergence of the deflection of a 3D beam for a passive Guccione-Costa-McCulloch material. Maximal vertical deflection with respect to the mesh resolution for different numerical schemes (a), and different values of the stabilisation constant (b).

ergy function proposed by Guccione et al. [15] (which is the material law used in the benchmark test from [26]): $\Psi_{\text{pas}} = a/2(e^Q - 1)$, with $Q = b_f E_{ff}^2 + b_t (E_{ss}^2 + E_{nn}^2 + E_{sn}^2 + E_{ns}^2) + b_{fs} (E_{fs}^2 + E_{sf}^2 + E_{fn}^2 + E_{nf}^2)$, where $a = 2$ kPa, $b_f = 8$, $b_t = 2$, $b_{fs} = 4$, and the E_{ij} denote entries of the Green-Lagrange strain tensor \mathbf{E} , rotated with respect to a local coordinate system aligned with f_0, s_0, n_0 . The beam is clamped at the face $x = 0$, a pressure of $p_N = 0.004$ kPa is imposed on the bottom face $z = 0$, and the remainder of the boundary is considered with traction-free conditions. According to (2.8b), the pressure boundary condition changes with the deformed surface orientation, and its magnitude scales with the deformed area. The outcome depicted in Figure 4(a) shows a rapid convergence of our first- and second-order methods, while the computations using a pressure-displacement formulation and the Taylor-Hood finite elements (continuous and piecewise quadratic approximations of displacements and continuous and piecewise linear approximations for pressure) display a somewhat slower convergence to the asymptotic deflection of the membrane. Using the unstable pair with discontinuous pressures (the $\mathbb{P}_2 - \mathbb{P}_1^{\text{disc}}$ pair) rectifies the convergence, but at a higher computational cost. The reference value is the average of the reported simulations from the study in [26]. Moreover, Figure 4(b) shows the vertical deflections as a function of the number of vertices discretising the small edge of the beam. The obtained results are consistent for varying values of the stabilisation parameter, ζ_{stab} , and the observed behaviour also confirms that our method is locking-free. These runs also justify our choice for the stabilisation parameter used in the subsequent examples.

4.4 Stress-assisted diffusion and conduction velocity assessment

In addition to determining a suitable parameter range for D_2 that ensures solvability of the discrete monodomain equations, we also investigated the effect of D_2 on the tissue's response to spiral wave dynamics. We compare the differences in the ionic quantities between simulations with a very small contribution of SAD ($D_2 = 1 \text{ E-}5 \text{ cm}^2/\text{s}$) and a more prominent (but still mild) SAD contribution encoded in the value $D_2 = 7.5\text{E-}3 \text{ cm}^2/\text{s}$. A closer inspection suggests that these contrasts were due to a difference in conduction velocity (CV) induced by SAD. In Figure 5(a,b), we see that conduction velocity was higher for larger values of D_2 (meaning a larger SAD contribution). When the wave first emerged, the peak action potential was more advanced for the case of reduced D_2 , but the large D_2 peak eventually caught up to and surpassed it, which is a phenomenon also observed in the active tension curves. The ionic quantities followed the same trend.

We also remark that the effect of changing conduction velocities was not spatially consistent. SAD increases CV in the fibre (horizontal) direction, but actually decreased CV in the vertical and diagonal directions. This resulted in a noteworthy effect on the growth of the spiral wave. Figures 5(c,d,e) show a comparison of the spiral wave in the viscoelastic case for three different values of D_2 . The upper right area

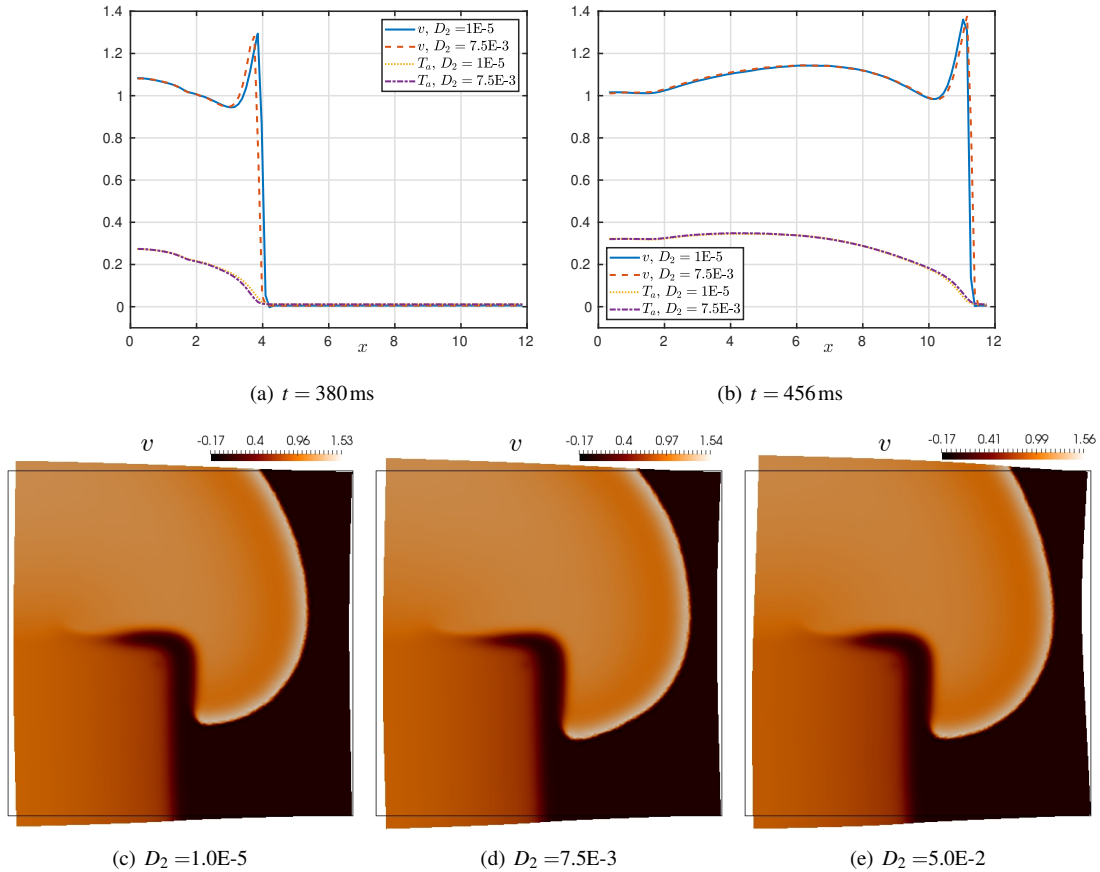


Fig. 5: (a,b): Propagation of action potential v and active tension T_a , measured by taking the profile over a horizontal line segment crossing the upper half of the tissue at $y = 7$ cm. Comparison is provided for two different values of D_2 . (c,d,e): Effect of D_2 on the potential wave at $t = 444$ ms in the viscoelastic case.

of the spiral is visibly flattened in the simulation with a larger value of D_2 , suggesting that propagation of the voltage was suppressed in that direction. A similar effect was seen in the viscoelastic case.

As in other studies, here we observe that conduction velocity is sensitive to spatio-temporal discretisation. In Table III, we include the results of a simple convergence test for conduction velocity, similar to the benchmark test conducted in [35]. We calculated the horizontal propagation of the action potential using different timesteps and mesh refinements. Differently than in the case of nonlinear diffusion without SAD from [35], the experiment reveals that lower resolutions produce larger CVs than the physiological values. This test also confirms that with our timestep and mesh resolution (0.1 ms, and above 200,000 DoF, respectively), conduction velocity is in the expected physiological range; whereas larger timesteps will systematically fail to capture the dynamics of the ionic model.

4.5 Scroll waves on mono-ventricular geometries

We start from patient-specific surface left ventricle geometries (available from [24, 40]) and rescaled using approximately the same dimensions as idealised ventricles studied in [35]. From there we define boundary labels and produce volumetric tetrahedral meshes of varying resolutions. The domain boundaries are set as sketched in Figure 1: The basal cut corresponds to $\partial\Omega_D$, the epicardium to $\partial\Omega_R$, where the Robin boundary conditions (2.8c) are defined with a spatially varying stiffness

$$\eta(y) = \frac{1}{y_b - y_a} [\eta_a(y_b - y) + \eta_b(y - y_a)],$$

Convergence of Conduction Velocity, cm/ms					
DoF	h	$\Delta t = 0.3$ ms	$\Delta t = 0.1$ ms	$\Delta t = 0.05$ ms	$\Delta t = 0.01$ ms
27038	0.3817 cm	0.1130	0.1032	0.1015	0.0994
108576	0.1909 cm	0.0754	0.0705	0.0654	0.0637
170919	0.1527 cm	0.0733	0.0657	0.0632	0.0620
246456	0.1273 cm	0.0701	0.0632	0.0601	0.0589
554960	0.0849 cm	0.0649	0.0553	0.0551	0.0550
1204362	0.0768 cm	0.0610	0.0552	0.0550	0.0547

TABLE III: Convergence of conduction velocity with respect to temporal and spatial discretisation.

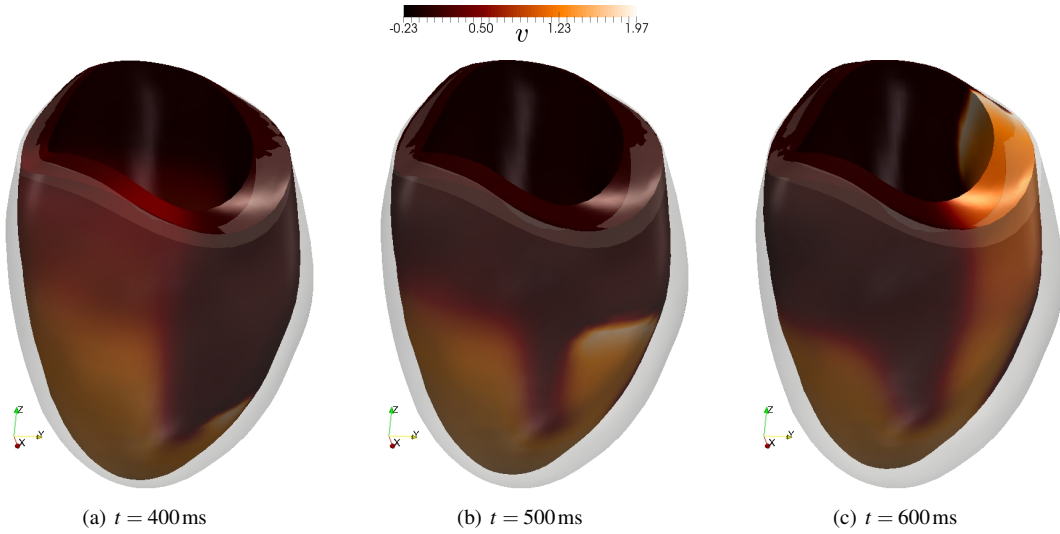


Fig. 6: Evolution of voltage after S2 stimulus (at $t = 335$ ms), showing formation of a scroll wave on a contracting ventricle. The shadow of the undeformed ventricle geometry is shown for comparison.

and the endocardium to $\partial\Omega_N$, where we set $p_N(t) = p_0 \sin^2(\pi t)$, representing the variation of endocardial pressure. The constants y_a, y_b are the vertical components of the apical and basal latitudes, and $\eta_a < \eta_b$ denotes the stiffness sought at the apex and base, respectively (assuming that the contact of the muscle with the aortic root is more resistant to traction than the more flexible pericardial sac and surrounding organs). In addition, since fibre and sheetlet fields for mono-ventricular geometries are not usually extracted from MRI data, we generate them using a mixed-form adaptation to the Laplace-Dirichlet rule-based method [35].

4.6 Effects due to viscoelasticity

In order to quantify the discrepancies between hyperelastic and viscoelastic effects we conduct a series of simulations using the coupled model on a 3D slab of dimensions $50 \times 50 \times 10$ mm³ using a fine mesh of $h = 0.25$ mm, and setting $f_0 = (1, 0, 0)^t$, $s_0 = (0, 1, 0)^t$. We apply a S1 stimulus on the face $x = 0$ and after $t = 92$ ms the propagation front has reached the state shown in Figure 7(a), plotted on the deformed configuration (which was computed with a full electro-viscoelastic model). At that time, in panels (b,c) we depict snapshots of the approximate solutions obtained using the hyperelastic and viscoelastic models with their base-line parameter values as reported in Table II, and shown over a line segment crossing the tissue slab parallel to the x -axis. We show profiles of the mechanical entities (x -components of displacement and pressure), as well as potential and r_3 . For reference, we also include the results obtained using a model without SAD contributions (that is with $D_2 = 0$). We can note that the curves produced without SAD are substantially lagged (as expected from the choice of diffusion parameters) with respect to the two

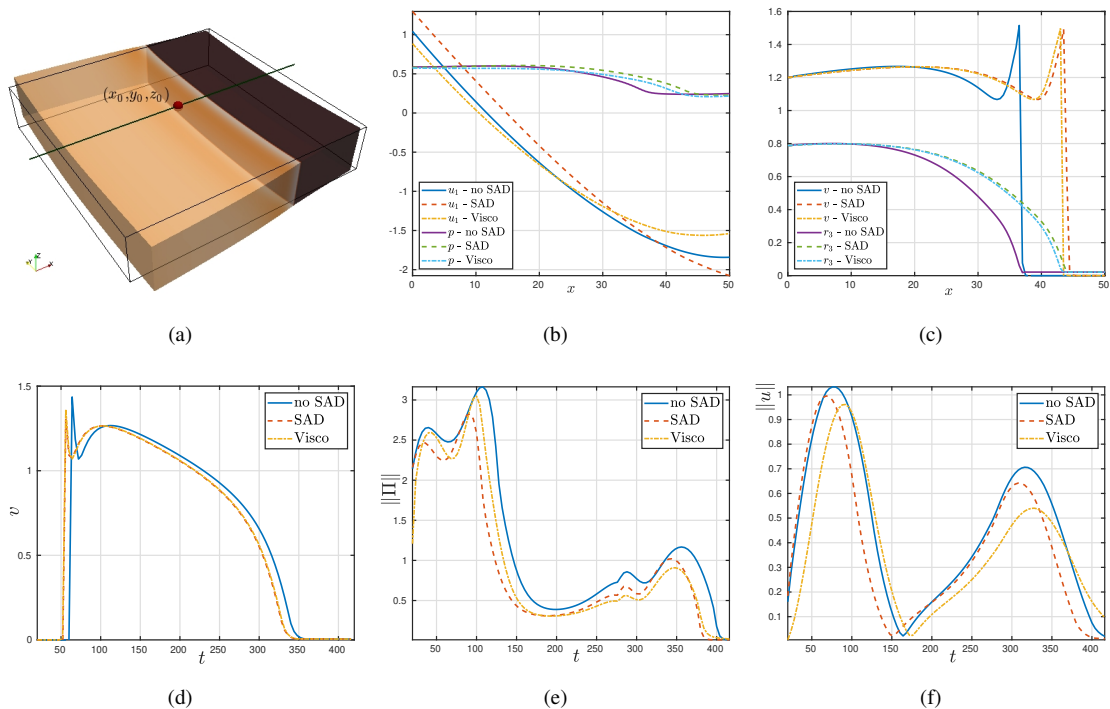


Fig. 7: Comparison of field variables between hyperelastic and viscoelastic cases on a line parallel to the x axis (sketched in (a)) taken at $t = 92$ ms (b,c); and point-wise evolution of field variables on the point (x_0, y_0, z_0) (d-i) for the cases of hyperelasticity without SAD, with the baseline case of SAD but without viscous stresses, and the viscoelastic case (line, dashed, and dashed-dotted curves, respectively).

other cases, that display no major discrepancies. The remaining of the panels in the figure show point-wise transients of the main mechanical and electrical fields measured on the point $(x_0, y_0, z_0) = (25, 25, 10)$. The evolution of the electric and activation fields remains very similar in all three cases, for instance the shape of the action potential is almost not modified after adding SAD or viscous contribution and for the other fields also very subtle differences are observed (the calcium concentration was slightly shifted to the left in the hyperelastic and viscoelastic cases). The changes are more pronounced in the transients of the mechanical quantities of the Frobenius norm of the Kirchhoff stress, the displacement magnitude and the pressure (panels g,h,i). These computations suggest that viscous effects will result in a decreased displacement, stress, and pressure (similar conclusions were drawn in [30], but not in the context of models for ventricular viscoelasticity). These discrepancies, however, are qualitatively small, and this observation was robust to every parameter combination that we tested, consistent spatially and in time. The application of a viscous model also had consequences related to performance. For instance, in the tests mentioned above, the average number of Newton iterations needed to reach convergence was systematically lower in the viscous case than in the hyperelastic case.

We next proceeded to investigate the effects of changing the viscosity parameters. The parameter β from (2.4) exerted minimal influence over the observed dynamics. Even for the five orders of magnitude tested, from $\beta = 0.1$ ms to $\beta = 10000$ ms, the differences in displacement, voltage, and all other variables were of less than 0.1%. This could be because of the low rates of change of deformation that we see in our simulations, or as a consequence of the adopted rheological model. We also tested values of δ across three orders of magnitude, from $\delta = 2.26$ to $\delta = 2260$ (in units $\text{N}/\text{cm}^2 \cdot \text{ms}$). As expected, increasing this quantity, thereby increasing the viscoelastic contribution to the Cauchy stress, magnified the differences between the hyperelastic and viscoelastic cases (essentially magnifying the effects seen in Figure 7). Additional simulations (not reported here) also shown that higher values of δ not only reduced the magnitude of Π , u , p , but also smoothed their profiles, reducing the distances between peaks and troughs. In the following we

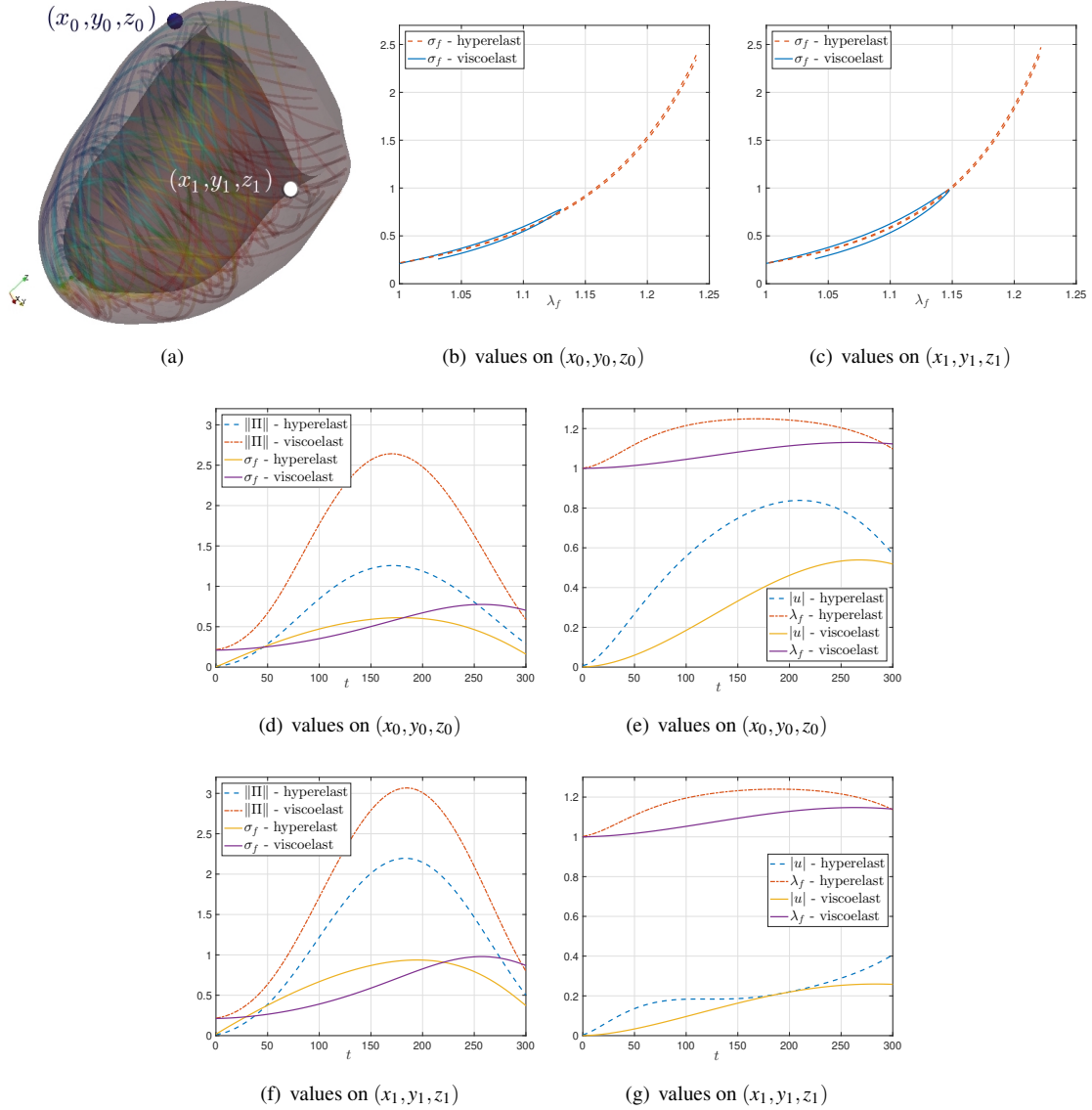


Fig. 8: Comparison between hyperelastic and viscoelastic true stress in the fibre direction $\sigma_f = \mathbf{F}f_0 \cdot (\sigma \mathbf{F}f_0)$, measured according to local stretch on two points on the epicardium (b) and endocardium (c) (points indicated in panel (a)). The plots in panels (d,e) show transients of mechanical outputs (Frobenius norm of the Kirchhoff stress, true stress on fibre direction, local stretch, and displacement magnitude) at the point (x_0, y_0, z_0) ; and plots (f,g) display their counterparts in point (x_1, y_1, z_1) .

will then restrict to $\beta = 1$ ms and $\delta = 22.6$ N/cm²·ms (and recall that we employ a timestep of $\Delta t = 0.1$ ms). These values, considered in [21] (and using units of [s] and [Pa s], respectively), ensure that the viscoelastic component is large enough to have a visible effect, but does not completely overwhelm the dynamics of the tissue.

Much more evident differences can be observed in terms of the true stress $\sigma_f = \mathbf{F}f_0 \cdot (\sigma \mathbf{F}f_0)$ when plotted against the local stretch in the fibre direction, $\lambda_f = \sqrt{I_{4,f}}$. Such a comparison has been conducted in [16] for idealised geometries, and it was specifically designed to study hysteresis effects due to viscous contributions to orthotropic passive stress. Here we consider the left ventricular domain used in Section 4.5 and proceed to analyse a stress-stretch response on two points near the basal surface on the endocardium and epicardium, and portrayed in Figure 8(a). The mechanical parameters were taken differently from those in Table II, here we focus on the patient-specific constants estimated from healthy myocardial tissue at 8

mmHg end-diastolic pressure using chamber pressure-volume and strain data taken in vivo [13]. The modified values for this particular test are $a = 0.02096 \text{ N/cm}^2$, $b = 3.243$, $a_f = 0.30634 \text{ N/cm}^2$, $b_f = 3.4595$, $a_s = 0.07334 \text{ N/cm}^2$, $b_s = 1.5473$, $a_{fs} = 0.03646 \text{ N/cm}^2$, $b_{fs} = 3.39$. In the simulation we impose a sinusoidal endocardial pressure of maximal amplitude 0.1 N/cm^2 (approximately 8 mmHg) and run a set of transient simulations over the interval from 0 to 300 ms. This configuration constitutes an inflation and deflation process where the majority of the fibres are acting in traction, whereas sheetlets work in compression regime. Plots (b,c) in Figure 8 illustrate the stress-stretch response (in terms of the true stress). The behaviour on the epicardial point shows an exponential stiffening and it is quite similar to what was observed in [16], as for both stress measures in the viscoelastic case we can evidence hysteresis effects (that are, by definition, not present in the hyperelastic case). Slight deviations from the reference results in [16] maybe related to the fact that we are using a full electromechanical model, a different viscoelastic contribution, and different material parameters.

5 Concluding remarks

We have introduced a new model for the active contraction of the cardiac muscle. We focused on incorporating the mechano-electrical feedback through a recent model of stress-assisted diffusion that also accounts for a porous-media-type of nonlinear diffusivity, also including inertial terms. The three-field equations of motion of a viscoelastic orthotropic material are coupled with a four-variable minimal model for human ventricular action potential using active stress. We have also proposed a new stabilised mixed-primal numerical scheme written, in particular, in terms of the discrete Kirchhoff stress. The nontrivial effects of both viscoelasticity and stress-assisted diffusion in our model suggest that they may play an important role in governing cardiac function and its response to external stimuli.

Readily apparent further additions to the present theoretical framework will be mostly focused on multi-scale microstructural coupling, this will provide a more sound multi-field justification of the model in terms of the complex phenomena involved in the cardiac mechano-electrical interaction. One example would be to include poroelastic effects representing perfusion of the myocardial tissue. Developing a thermodynamically consistent description of stress-assisted diffusion is also a pending task, in which electromechanical coupling with the surrounding torso and organs would represent another level of investigation. In particular, a generalised mechanical bidomain formulation, accounting for nonlinear and stress-assisted diffusion, will require state-of-the-art tools of multiscale homogenisation, as well as dedicated multiscale numerical methods.

References

- [1] M.S. ALNÆS, J. BLECHTA, J. HAKE, A. JOHANSSON, B. KEHLET, A. LOGG, C. RICHARDSON, J. RING, M.E. ROGNES, AND G.N. WELLS, *The FEniCS project version 1.5*, Arch. Numer. Softw. (2015), **3(100)**:9–23.
- [2] D. BAROLI, A. QUARTERONI, AND R. RUIZ-BAIER, *Convergence of a stabilized discontinuous Galerkin method for incompressible nonlinear elasticity*, Adv. Comput. Math. (2013), **39**:425–443.
- [3] A. BUENO-OROVIO, E.M. CHERRY, AND F.H. FENTON, *Minimal model for human ventricular action potential in tissue*, J. Theor. Biol. (2008), **253**:544–560.
- [4] B. CANSIZ, H. DAL, AND M. KALISKE, *Computational cardiology: A modified Hill model to describe the electro-visco-elasticity of the myocardium*, Comput. Methods Appl. Mech. Engrg. (2017), **315**:434–466.
- [5] K.S. CHAVAN, B.P. LAMICHHANE, AND B.I. WOHLMUTH, *Locking-free finite element methods for linear and nonlinear elasticity in 2D and 3D*, Comput. Methods Appl. Mech. Engrg. (2007), **196**:4075–4086.
- [6] C. CHERUBINI, S. FILIPPI, A. GIZZI, AND R. RUIZ BAIER, *A note on stress-driven anisotropic diffusion and its role in active deformable media*, J. Theoret. Biol. (2017), **430(7)**:221–228.
- [7] P.G. CIARLET, *Mathematical Elasticity Vol. 1: Three-dimensional Elasticity*, North Holland, Amsterdam, 1988.

- [8] P. COLLI FRANZONE, L.F. PAVARINO, AND S. SCACCHI, *Mathematical Cardiac Electrophysiology*, Springer MS&A, Heidelberg (2014).
- [9] P. COLLI FRANZONE, L.F. PAVARINO, AND S. SCACCHI, *Bioelectrical effects of mechanical feedbacks in a strongly coupled cardiac electro-mechanical model*, *Math. Models Methods Appl. Sci.* (2016), **26**:27–57.
- [10] F.S. COSTABAL, F.A. CONCHA, D.E. HURTADO, AND E. KUHL, *The importance of mechano-electrical feedback and inertia in cardiac electromechanics*, *Comput. Methods Appl. Mech. Engrg.* (2017), **320**:352–368.
- [11] N. CUSIMANO, A. BUENO-OROVIO, I. TURNER, AND K. BURRAGE, *On the order of the fractional Laplacian in determining the spatio-temporal evolution of a space-fractional model of cardiac electrophysiology*, *J. Comput. Phys.* (2018), **10**:e0143938.
- [12] F. DORRI, P.F. NIEDERER, AND P.P. LUNKENHEIMER, *A finite element model of the human left ventricular systole*, *Comput. Methods Biomech. Biomed. Engrg.* (2006), **9**(5):319–341.
- [13] H. GAO, W.G. LI, L. CAI, C. BERRI, AND X.Y. LUO, *Parameter estimation in a Holzapfel–Ogden law for healthy myocardium*, *J. Engr. Math.* (2015), **95**:231–248.
- [14] S. GÖKTEPE, A. MENZEL, AND E. KUHL, *Micro-structurally based kinematic approaches to electromechanics of the heart*, In *Computer Models in Biomechanics*. Springer Netherlands, (2013), pp. 175–187.
- [15] J.M. GUCCIONE, K.D. COSTA, AND A.D. MCCULLOCH, *Finite element stress analysis of left ventricular mechanics in the beating dog heart*, *J. Biomech.* (1995), **28**:1167–1177.
- [16] O. GÜLTEKIN, G. SOMMER, AND G.A. HOLZAPFEL, *An orthotropic viscoelastic model for the passive myocardium: continuum basis and numerical treatment*, *Comput. Meth. Biomech. Biomed. Engrg.* (2016), **19**(15):1647–1664.
- [17] M. HADJICHARALAMBOUS, J. LEE, N.P. SMITH, AND D.A. NORDSLETTEN, *A displacement-based finite element formulation for incompressible and nearly-incompressible cardiac mechanics*, *Comput. Methods Appl. Mech. Engrg.* (2014), **274**:213–236.
- [18] G.A. HOLZAPFEL AND T.C. GASSER, *A viscoelastic model for fiber-reinforced composites at finite strains: Continuum basis, computational aspects and applications*, *Comput. Methods Appl. Mech. Engrg.* (2001), **190**(34):4379–4403.
- [19] G.A. HOLZAPFEL AND R.W. OGDEN, *Constitutive modelling of passive myocardium: a structurally based framework for material characterization*, *Phil. Trans. Royal Soc. London A* (2009), **367**:3445–3475.
- [20] D. HURTADO, S. CASTRO, AND A. GIZZI, *Computational modeling of non-linear diffusion in cardiac electrophysiology: A novel porous-medium approach*, *Comput. Methods Appl. Mech. Engrg.* (2016), **300**:70–83.
- [21] K.S. KARLSEN, *Effects of inertia in modeling of left ventricular mechanics*, Master thesis in Mathematics. University of Oslo, 2017.
- [22] L. KATSNELSON, L.V. NIKITINA, D. CHEMLA, O. SOLOVYOVA, C. COIRAULT, Y. LECARPENTIER, AND V.S. MARKHASIN, *Influence of viscosity on myocardium mechanical activity: a mathematical model*, *J. Theoret. Biol.* (2004), **230**:385–405.
- [23] D. KLEPACH AND T.I. ZOHDI, *Strain assisted diffusion: Modeling and simulation of deformation-dependent diffusion in composite media*, *Composites B: Engrg.* (2014), **56**:413–423.
- [24] P. LAMATA, *Computational meshes of the cardiac left ventricle of 50 heart failure subjects*, online dataset (2018), DOI:10.6084/m9.figshare.5853948.v1.
- [25] B.P. LAMICHHANE AND E.P. STEPHAN, *A symmetric mixed finite element method for nearly incompressible elasticity based on biorthogonal systems*, *Numer. Methods PDEs* (2012), **28**(4):1336–1353.
- [26] S. LAND, ET AL., *Verification of cardiac mechanics software: benchmark problems and solutions for testing active and passive material behaviour*, *Proc. R. Soc. A.* (2015), **471**(2184):20150641.

- [27] P. LENARDA, A. GIZZI, AND M. PAGGI, *A modeling framework for electro-mechanical interaction between excitable deformable cells*, Eur. J. Mech.-A/Sol. (2018), **72**:374–392.
- [28] A. LOPPINI, A. GIZZI, R. RUIZ-BAIER, C. CHERUBINI, F.H. FENTON, AND S. FILIPPI, *Competing mechanisms of stress-assisted diffusivity and stretch-activated currents in cardiac electromechanics*, Front. Physiol. (2018), **9**:1714.
- [29] F. NOBILE, R. RUIZ-BAIER, AND A. QUARTERONI, *An active strain electromechanical model for cardiac tissue*, Int. J. Numer. Methods Biomed. Engrg. (2012), **28**:52–71.
- [30] A. PANDOLFI, A. GIZZI, AND M. VASTA, *Visco-electro-elastic models of fiber-distributed active tissues*, Meccanica (2017), **52**:3399–3415.
- [31] S. PEZZUTO, D. AMBROSI, AND A. QUARTERONI, *An orthotropic active-strain model for the myocardium mechanics and its numerical approximation*, Eur. J. Mech. A/Solids (2014), **48**:83–96.
- [32] A. QUARTERONI, T. LASSILA, S. ROSSI, AND R. RUIZ-BAIER, *Integrated heart – coupled multiscale and multiphysics models for the simulation of the cardiac function*, Comput. Methods Appl. Mech. Engrg. (2017), **314**:345–407.
- [33] S. ROSSI, T. LASSILA, R. RUIZ-BAIER, A. SEQUEIRA, AND A. QUARTERONI, *Thermodynamically consistent orthotropic activation model capturing ventricular systolic wall thickening in cardiac electromechanics*, Eur. J. Mech. A/Solids (2014), **48**:129–142.
- [34] R. RUIZ-BAIER, *Primal-mixed formulations for reaction-diffusion systems on deforming domains*, J. Comput. Phys. (2015), **299**:320–338.
- [35] R. RUIZ-BAIER, A. GIZZI, A. LOPPINI, C. CHERUBINI, AND S. FILIPPI, *Thermo-electric effects in an anisotropic active-strain electromechanical model*, Comm. Comput. Phys. (2018), submitted.
- [36] G. SCOVAZZI, B. CARNES, X. ZENG, AND S. ROSSI, *A simple, stable, and accurate linear tetrahedral finite element for transient, nearly, and fully incompressible solid dynamics: a dynamic variational multiscale approach*, Int. J. Numer. Methods Engrg. (2016), **106(10)**:799–839.
- [37] J. SUNDNES, S. WALL, H. OSNES, T. THORVALDSEN, AND A.D. MCCULLOCH, *Improved discretisation and linearisation of active tension in strongly coupled cardiac electro-mechanics simulations*, Comput. Meth. Biomech. Biomed. Engrg. (2014), **17(6)**:604–615.
- [38] T.P. USYK, R. MAZHARI, AND A.D. MCCULLOCH, *Effect of laminar orthotropic myofiber architecture on regional stress and strain in the canine left ventricle*, J. Elast. (2000), **61**:143–164.
- [39] J. YAO, V.D. VARNER, L.L. BRILLI, J.M. YOUNG, L.A. TABER, AND R. PERUCCHIO, *Viscoelastic material properties of the myocardium and cardiac jelly in the looping chick heart*, J. Biomech. Engrg. (2012), **134(2)**:024502.
- [40] D.R. WARRINER, T. JACKSON, E. ZACUR, E. SAMMUT, P. SHERIDAN, D. ROD HOSE, P. LAWFORDE, R. RAZAVI, S.A. NIEDERER, C.A. RINALDI, AND P. LAMATA, *An asymmetric wall-thickening pattern predicts response to cardiac resynchronization therapy*, JACC: Cardio. Imag. (2018), **11(10)**:1545–1546.